

MEASUREMENTS OF SOLAR MAGNETIC ELEMENT MOTION FROM HIGH-RESOLUTION FILTERGRAMS

THOMAS E. BERGER, MATS G. LÖFDAHL,¹ RICHARD S. SHINE, AND ALAN M. TITLE
Lockheed-Martin Advanced Technology Center, O/H1-12, B/252, 3251 Hanover Street, Palo Alto, CA 94304

Received 1997 April 8; accepted 1997 October 7

ABSTRACT

Solar photospheric flowfield properties on sub-0.5 scales are measured using local correlation tracking (LCT) and object tracking of magnetic bright points (MBPs: photospheric bright points associated with magnetic elements). The dataset is a 70 minute time series of cospatial and cotemporal *G*-band 4305 Å and wideband 4686 Å filtergrams obtained with the 50 cm Swedish Vacuum Solar Telescope on the island of La Palma, Spain. We examine a 29" × 70" field of view (FOV) near disk center and compare a 29" × 29" magnetic network subfield and a 27" × 27" apparently nonmagnetic "quiet-Sun" subfield. The mean time between frames is 23.75 s. Each frame is created by partitioned phase-diverse speckle restoration of three image pairs acquired rapidly in sequence. Angular resolution is ~0.4 or less in all frames of the restored data set.

From LCT on a 0.4 grid with 0.83 FWHM apodization, we find the flow speeds to be Rayleigh distributed with a mode of 550 m s⁻¹ and an average of 950 m s⁻¹ in the network FOV; in the quiet FOV the modal speed is 700 m s⁻¹ with a mean of 1100 m s⁻¹. Within the network FOV, a "magnetic region" defined by the loci of tracked MBPs exhibit even greater alteration: rms contrast of the region is 8% higher in the *G* band compared to areas outside, LCT speeds are reduced by a factor of 1.6, and the convective flow structures are smaller and much more chaotic. Mesogranulation is entirely absent in the magnetic region. The modal and mean speeds of 534 tracked MBPs are 300 m s⁻¹ and 1470 m s⁻¹, respectively. MBPs split and merge with mean times of 320 and 404 s respectively. The mean lifetime of MBPs in the data set is 9.33 minutes although approximately 5% of the objects can be tracked for the entire 70 minute duration of the time series.

Subject headings: Sun: magnetic fields — Sun: faculae, plages — Sun: photosphere —
techniques: image processing

1. INTRODUCTION

Magnetic elements are high field-strength, subgranular scale, concentrations of magnetic flux in the photosphere. They are by definition the smallest resolvable structures in the solar magnetic network. Magnetograph measurements and empirical modeling techniques (Solanki 1993; Rabin 1992; Keller et al. 1990; Zayer, Solanki, & Stenflo 1989; Stenflo 1973) have established a range in magnetic element field strengths of 1200–2000 G. Given the critical role of magnetic element dynamics in imparting energy to higher atmospheric levels (Parker 1990), quantitative measurements of the speeds, lifetimes, ranges, and interaction frequencies of magnetic elements are of great interest. However, the small scale of magnetic elements and the relatively long exposures required for magnetograms have prevented study of their dynamics and evolution in relation to the photospheric flowfield.

The most detailed information on magnetic element dynamics has come from tracking associated radiative indicators in the photosphere such as continuum and molecular-band bright points. Berger et al. (1995a), following on the work of Muller & Mena (1987), demonstrate that bright points are seen with particularly high contrast with particularly high contrast seen in filtergrams taken in the *G*-band region of the solar spectrum (a band head of the CH

radical near 4300 Å). The characteristic observed size of both *G*-band and continuum bright points is about 250 km (0.35; Berger et al. 1995a; Muller 1994; Auffret & Muller 1991; Muller & Keil 1983; Spruit & Zwaan 1981; Mehlretter 1974; Dunn & Zirker 1973). Title & Berger (1996) show that, in addition to the use of a good bandpass filter, a spatial resolution of 0.4 or better is required for successful study of photospheric bright points. Even with this resolution, the measured bright point sizes will be nearly a factor of 2 larger than the actual diameters due to averaging with the surrounding dark intergranular lanes (Title & Berger 1996). Berger (1996) demonstrates an image segmentation algorithm that is able to identify (to a statistical certainty of greater than 84%) *G*-band bright points which occur *only* at sites of magnetic flux as measured in cotemporal magnetograms. We report here an improvement to the segmentation algorithm which, although we lack a cotemporal magnetogram to quantify the effect, should significantly increase the correlation. We hereafter refer to *G*-band bright points identified by our segmentation algorithm as "magnetic bright points (MBPs)."

Preliminary studies of MBP dynamics find that they undergo a continual merging and fragmentation evolution with mean speeds on the order of 1–2 km s⁻¹ (Berger & Title 1996; Muller et al. 1994; Roudier et al. 1994). However, these findings are limited by their reliance on manual tracking of bright points: the low number of objects tracked and inherent selection effects limit the applicability of the conclusions. To establish a good statistical measure of MBP dynamics, a large number of objects must be

¹ Large parts of this analysis were performed while M. G. L. was with the Royal Swedish Academy of Sciences, Stockholm Observatory, S-133 36 Salsjöbaden, Sweden.

tracked using an unbiased automated tracking algorithm. This, in turn, requires a dataset consisting of a relatively large field of view to capture many separate bright points (on the order of 30" or more), very high spatial resolution which is *consistent* in all images of the dataset, a frame rate which captures the dynamics of bright points on ~ 100 s timescales, and a temporal length sufficient to discern the evolution of the bright points in relation to meso- and supergranular flows (on the order of hours). The acquisition of such a data set has recently become practical through the application of phase diversity image restoration (see Löfdahl & Scharmer 1994 and references therein) to very high quality ground-based solar image sequences.

This paper reports the first of several analyses of a new phase diversity restored data set suitable for magnetic element dynamics studies. The primary data set is a 70 minute time series of *G*-band filtergrams taken at the 50 cm Swedish Vacuum Solar Telescope (SVST) on the island of La Palma, Spain. A second time series of 4686 Å wideband² filtergrams, cospatial and simultaneous to within 10 ms with the *G*-band images, is also studied. The full field of view (FOV) consists of a 29" \times 70" area near Sun center which includes a region of enhanced network activity showing hundreds of *G*-band bright points. Both time series are restored to very near the telescope diffraction limit (0.2" in the *G*-band) by a particular variation of phase diversity restoration called partitioned phase diverse speckle (PPDS).

Section 2 discusses in some detail the issues pertaining to using *G*-band bright points as surrogates in magnetic element studies. Section 3 briefly summarizes the observations. The details of the observations and the PPDS restorations are given in a parallel paper (Löfdahl et al. 1998, hereafter Paper I). Section 4 details the reduction of the restored data sets into time series suitable for local correlation tracking (LCT; Bogart et al. 1988; November & Simon 1988; November 1986; Tarbell, Title, & Schoolman 1979) and bright point object tracking. Section 5 presents analyses of photospheric flowfield properties both within and outside the enhanced network region. The analyses are split into three areas: we first examine the larger scale motions of magnetic element *patterns* in the enhanced network region. The radiant intensity of a defined "magnetic region" relative to the surrounding "quiet" granulation in both the *G*-band and 4686 Å bandpass is also examined. Second, we measure the flow-field properties on LCT grids as small as 0.4". Third, we analyze the motions of over 500 magnetic elements via automated tracking of MBPs.

2. *G*-BAND BRIGHT POINTS AND THE PHOTOSPHERIC MAGNETIC FIELD

As stated above, Berger (1996) establishes to a high degree of statistical certainty that *G*-band bright points identified with a particular image segmentation algorithm occur only at sites of magnetic flux. However, the same study, as well as many others (Berger et al. 1995b; Yi & Engvold 1993; Keller 1992; Title et al. 1990; Muller 1985; Mehlretter 1974), show that magnetic elements can often be found without discernible associated bright points. In short, magnetic flux is a necessary, but not sufficient, condi-

tion for the occurrence of photospheric bright points. In addition, there is evidence that continuum bright points may occur in the absence of detectable magnetic flux (Beckers & Schröter 1968; Keller 1993). Both of these points emphasize that we do not fully understand the physics of radiative transfer through magnetic elements in the photosphere. Using bright points to track magnetic elements therefore requires attention to possible biases in the analyses. We address the main biases in the following paragraphs and find that measurement of magnetic element dynamics using bright points must be interpreted with care.

One difficulty in using bright points as magnetic element tracers is the possibility that "nonmagnetic bright points" may be included in the flow measurements and effect the statistics. Berger (1996) finds that using image segmentation algorithms based solely on *G*-band image data to identify bright points results in $\sim 15\%$ – 20% of the objects being false identifications (as judged by manual inspection). The large majority of these false bright points are found to be localized brightenings on granular edges. In the current study we employ an improved algorithm based on multi-wavelength image data which lowers the false identification level to less than 5%. Even at the 5% level, granulation peaks in the tracking data could bias the value of the average measured speed if their flow character was sufficiently different from that of true bright points. However, as pointed out in Berger & Title (1996), the dynamics of granulation at the intergranular lane boundaries and the dynamics of bright points are closely related. Therefore, the distortion of statistical distributions of speed and other flow-field characteristics due to false bright points is expected to be negligible.

Regardless of the fraction of real bright points tracked by our algorithm, the results are still obviously biased to those magnetic elements which have associated *G*-band bright points at any time during the observation period. It is possible that the dynamic character of "illuminated" magnetic elements differs from that of "invisible" magnetic elements. However, this is unlikely since the kinetic energy of the photospheric flow field far exceeds the radiative losses associated with bright point formation in any bandpass. Still this bias is an inherent property of our analysis, the magnitude of which can only be addressed in a suitable *G*-band/magnetogram data set; by using only *G*-band bright points to locate and track magnetic elements, our measurements may be limited to some sub-class of the small-scale magnetic field.

It is also possible that bright points occur only at some particular region of the associated magnetic element (the central core for instance). If so, the evolution of the bright point may not be exactly the same as the magnetic field itself. But consideration of the size scales under investigation makes this unlikely as well. Magnetic elements are located in intergranular lanes; the large majority of the *G*-band bright points we observe nearly fill the intergranular lanes in which they reside; therefore, it is highly improbable that the associated magnetic elements are significantly larger than the bright points under investigation. When a given bright point undergoes a fragmentation in which the fragments move at least a diameter apart, this indicates to a high probability that the underlying magnetic element has similarly undergone a fragmentation. In the same way, the merging of two bright points most probably indicates the coalescence of the associated magnetic flux.

² See § 3 for a detailed description of the bandpass.

Lastly, the temporal relation of *G*-band bright points to the associated magnetic element is uncertain. Berger & Title (1996) point out that fragmentation of a magnetic element may result in associated *G*-band bright points that are below the telescope resolution limit which appear to vanish while the magnetic flux remains. In addition, Berger (1996) finds cases in which *resolved* *G*-band bright points fade out while the associated magnetic elements remain detectable in cotemporal magnetograms. Bright points can also apparently “turn-on” and/or intensify when the associated magnetic element is compressed or concentrated in a granular vertex area (Muller & Roudier 1992). All these findings imply that measurements of bright point lifetime are *not* applicable to the associated magnetic flux. However, we assume here that such temporal quantities as the mean times between bright point splittings or mergers are applicable to the underlying magnetic elements because we observe the entire processes of splitting and merging.

In summary, using bright points to track magnetic elements introduces several biases which may limit the generality of the results. Nevertheless, until magnetogram temporal and spatial resolutions are very much increased, bright point tracking is the best method for studying the dynamics and evolution of the small-scale magnetic field in relation to photospheric flows.

3. OBSERVATIONS

The observations and image restoration procedures are described in detail in Paper I. In brief, phase-diverse data were collected with the 50 cm Swedish Vacuum Solar Telescope (SVST) on 1995 October 5 between 10:57 and 12:08 UT. An area of both quiet Sun and enhanced network activity (exhibiting hundreds of *G*-band bright points) near disk center was observed using two Kodak Megaplug 1.6 1536×1032 pixel 10 bit CCD cameras. One camera used a 12 Å bandpass *G*-band interference filter (center wavelength 4305 Å) and the other used a 54 Å bandpass interference filter (center wavelength 4686 Å). The latter filter is referred to as the “wideband” filter to distinguish it from the *G*-band filter; it produces images of the photosphere which appear somewhat like those that narrowband continuum filters produce (see Title et al. 1992). In particular, magnetic elements do not show more than 3–6% contrast in this bandpass whereas the average magnetic element contrast in the *G*-band is between 20%–30% (Berger et al. 1995a). The image scale in both filter channels is $0''.083 \text{ pixel}^{-1}$; the diffraction limited (λ/D) resolution is $0''.228$ in the *G* band and $0''.248$ in the 4686 Å channel. The shutters of both cameras were synchronized by computer; the integration time was 20 ms. Real-time frame selection on a 25 s cadence was carried out on the *G*-band camera; the best three *G*-band frames from each 20 s evaluation period, *and* the simultaneous wideband frames, were recorded for phase diversity processing. Figure 1 of Paper I, shows the optical arrangement. Ca II K-line images were also recorded but have not been analyzed for this paper.

Both cameras were equipped with phase diversity beam splitters (see Fig. 2 in Paper I) which put two images on each CCD with a difference in focus position corresponding to 8.85 mm (± 0.1 mm) in air. This is equivalent to 1.16 and 1.06 waves peak-to-peak defocus in the *G*-band and wideband channels, respectively. The necessity of recording two simultaneous images of the same FOV on a single CCD

chip results in a large aspect ratio for the images: the restored FOV for both wavelengths is $29'' \times 70''$.

4. DATA REDUCTION

Both the *G*-band and wideband raw images are photometrically corrected by CCD dark current subtraction and flat-fielding prior to PPDS restoration. Following PPDS restoration, the time series are further processed by rigidly aligning images in the sequence to remove telescope pointing jitter. Image rotation due to the altitude-azimuth mount of the SVST is also removed by regridding with bilinear interpolation. Geometric distortions between image pairs induced by atmospheric seeing are removed by a temporally filtered “destretching” of images. Finally, intensity variations in the time series due to *p*- and *f*-mode solar acoustic oscillations are removed by Fourier filtering in spatial-temporal frequency (k - ω) space. The particular filter used is a sharp-edged linear filter in k - ω with a slope equivalent to 4 km s^{-1} in x - t space. In addition to successfully removing the *p*- and *f*-mode oscillations, this filter also (undesirably) attenuates surface flow motions above the 4 km s^{-1} threshold, introducing some temporal “smearing” of fast motions in the dataset.

An example of a fully processed, full FOV, *G*-band image is shown in Figure 6 of Paper I. The upper portion of the FOV consists of relatively nonmagnetic (“quiet”) granulation while the lower portion contains the enhanced network region. The white squares demarcate subregions which are analyzed individually in later sections for magnetic field concentration effects. The upper square is $26''.7 \times 26''.7$ and encloses only quiet granulation; we define this region as the “quiet FOV.” The lower square is $29''.2 \times 29''.2$ and encloses most of the enhanced network activity; we define this region as the “network FOV.” The fully processed network FOV in both *G*-band and 4686 Å bandpasses is shown in Figure 1 (Plate 26).

Magnetic elements are easily identified by eye in *G*-band images such as the one shown in Figure 1, but their unambiguous identification by computer is less straightforward due to confusion with localized peaks near granule edges. In the current data set, the inclusion of simultaneous wideband images improves discrimination of the false granulation peaks from MBPs greatly. Figure 2 (Plate 27) shows the result of subtracting the wideband image from the *G*-band image for the network FOV shown in Figure 1. As initially shown by Göran Scharmer of the SVST, the granulation in the two images cancels almost completely due to the synchronization of the exposures. However, the much higher contrast of MBPs in the *G* band relative to the wideband leaves them clearly visible. In addition to the obvious (and expected) enhancement of the bright points in the subtraction image, there is an excess of *G*-band brightness relative to the wideband brightness distributed in a diffuse manner around and in between the bright points. This “diffuse component” of *G*-band brightness has not previously been recognized. From examination of the time series, it is clear that the diffuse component can occur and evolve independently from nearby bright points leading us to believe that it is not an artifact of the image restoration or processing.

The MBP and diffuse *G*-band components belong to a distinct distribution of pixel intensity relative to the granulation. For example, Figure 3 plots *G*-band pixel contrast (intensity relative to the image mean intensity) against the

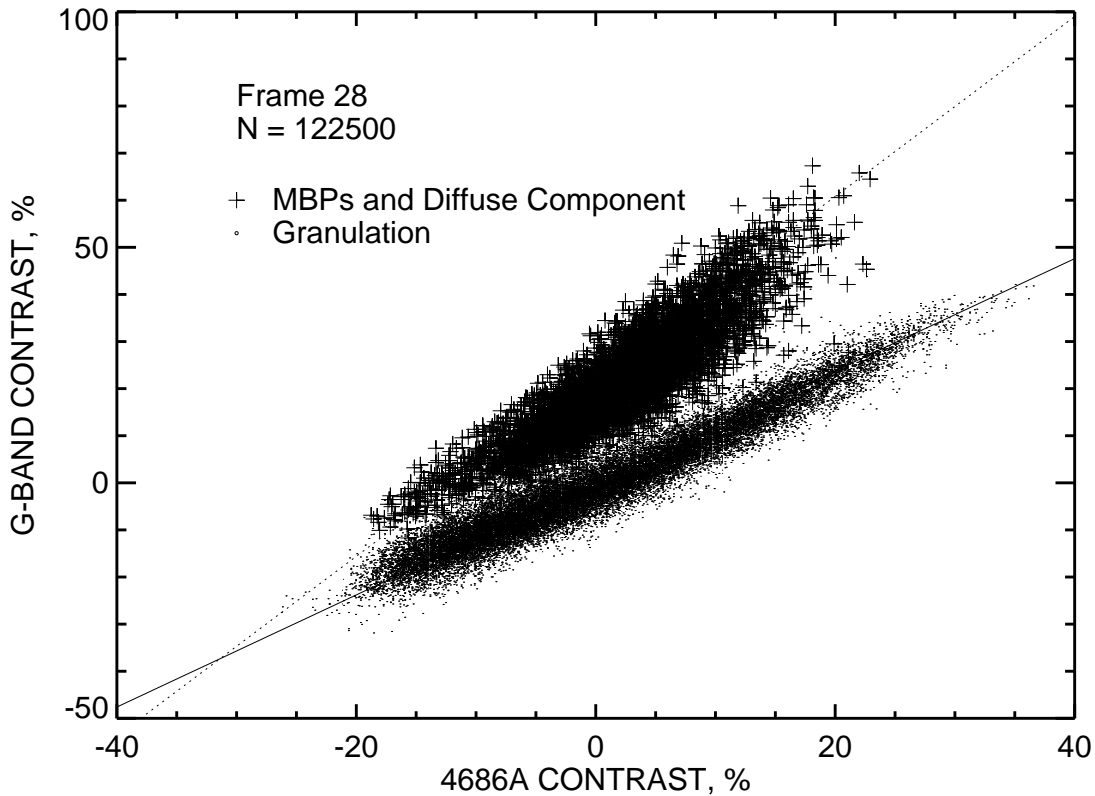


FIG. 3.—Contrast scatterplot of PPDS restored frame 28 (11:08 UT). All 122,500 pixels from the network FOV of the G -band and 4686 Å wideband images are plotted. Using the automated segmentation algorithm described in the text, all G -band bright point pixels, as well as all pixels exhibiting the “diffuse” G -band component, have been marked in the plot by crosses (*upper distribution*). The remaining pixels in the lower distribution (*plotted as points*) are found to be granulation. The least-squares fits to the magnetic and granulation distributions cited in eq. (1) are shown as solid lines.

4686 Å wideband pixel contrast for the single image pair shown in Figure 1. Two relative contrast distributions are discernible in the plot. By inspection, we find that the upper distribution (*crosses*) is due *only* to the MBPs and diffuse component while the lower distribution (*points*) is due to the remaining pixels in the image. The distributions in Figure 3 are fitted with the following least-squares linear regressions:

$$\begin{aligned} C_{4305} &= 1.91 C_{4686} + 22.6 \quad \text{MBP/diffuse,} \\ C_{4305} &= 1.19 C_{4686} \quad \text{granulation,} \end{aligned} \quad (1)$$

where C_{4305} and C_{4686} are the G -band and wideband contrasts in percent, respectively. Similar relations are found for all G -band/4686 Å image pairs in the data set. Equation (1) indicates that while the granulation in the images scales linearly with zero offset between wavelengths, the MBP/diffuse component has both a scaling factor and a constant enhancement in the G band. The $\sim 23\%$ contrast enhancement of this component in the G band agrees well with the 20% value found in an earlier study which analyzed magnetic element contrast in simultaneous G -band and 6302 Å continuum images (Berger 1996).

Given the bimodal behavior of the image contrast distributions seen in Figure 3, segmenting MBPs from the images becomes a simple three-step process: first, a binary image is produced from a thresholded version of the G -band brightness density map (Berger et al. 1995a). Second, a binary image in which all pixels above a threshold in the G -band/wide band difference image are set to 1 and the remainder are set to zero is produced. This step selects only those pixels in the MBP/diffuse distribution in Figure 3 and results in a MBP/diffuse component binary map. Finally,

the two binary maps are combined in a boolean “and” operation to eliminate most granule peaks and produce an MBP binary map. The percentage of falsely identified pixels in several MBP maps was checked manually and found to be below 5% in all cases. The majority of the false objects contain fewer than 5 pixels; objects consisting of fewer than 5 pixels are therefore excluded from further analysis. While this introduces a bias in the analyses towards objects larger than this threshold, the threshold is close enough to the spatial resolution limit of the instrumentation that the bias is not a significant concern.

All bright point maps are produced from the G -band time series prior to p -mode attenuation in order to avoid the implicit interpolation inherent in the filtration process. Since these maps are used in the magnetic element tracking procedure, this also avoids attenuation of real motions which may exceed 4 km s^{-1} . The bright point map produced from the network region of frame 28 of the data set (see Fig. 1) is shown subtracted from both the G band and the difference images in Figure 4 (Plate 28). The subtraction of the bright point map from the difference image highlights the diffuse G -band “emission” found in the difference images. The number of pixels in the bright point map for frame 28 represents 3% of the total image area. Including the diffuse component, the total area increases to 4.5% of the FOV.

5. ANALYSES

5.1. Large-Scale Characteristics

The G -band time series reveals that the while individual magnetic elements are in constant random motion, the

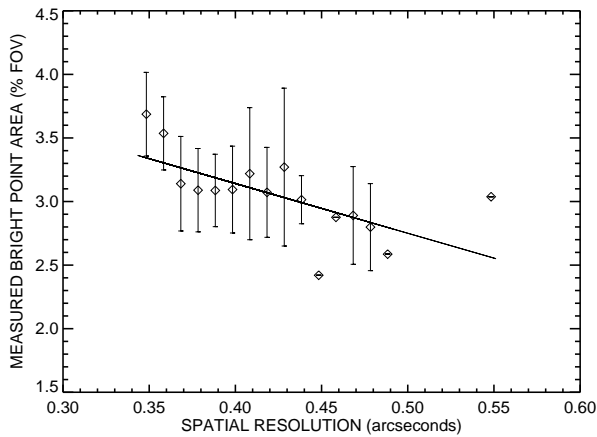


FIG. 6.—Total bright point area (normalized to image area) as a function of the spatial resolution of the PPDS restored image. Spatial resolution is defined from the maximum width of the spatial frequency filter, U_H , used in the PPDS image restoration (see Paper I for details). The data are grouped in $0^{\circ}01$ bins; the diamond symbols show the bin averages and the error bars are $\pm 1 \sigma$. The straight line is a least-squares fit to the full (unbinned) data.

large-scale pattern of magnetic elements remains fairly constant throughout the time series. For example, certain areas in the network contain clusters made up of several magnetic elements which typically move, fragment, merge, disappear, and reappear all within a radius of a few arcseconds.

These clusters are best exhibited in time-summed images created by coadding many frames of the *G*-band bright point mask images together. Two such images are shown in Figure 5 (Plate 29). Color coding of the images shows present and past locations of bright points: past locations (trails) of MBPs are shown in dark blue, while the current locations of MBPs, corresponding to the last image in the time sum are shown in light blue. Figure 5*a* is the sum over the first ~ 12 minutes of the time series and Figure 5*b* shows the sum over the entire 70 minutes of the time series. The final area fraction of the FOV covered by MBP tracks is 26%. In the image of Figure 5*b*, clusters are noticeable as “islands” disconnected from the larger area covered by magnetic element tracks.

As mentioned in the previous section, in any one bright point mapping, the fraction of the FOV covered by identified MBPs is approximately 3%. However, residual seeing effects result in differing spatial resolutions throughout the time series. It is of interest to quantify the range of variation of measured bright point area as a function of spatial resolution of the observations. As discussed in Paper I, residual seeing effects can be quantified in the form of varying maximum spatial frequencies achieved in the PPDS restoration. The effect of restored *G*-band image spatial resolution on the measured bright area is shown in Fig. 6 for all frames in the data set. Although the general trend (shown by the least-squares linear fit to the unbinned data) clearly shows decreasing measured bright point area with decreasing spatial resolution, the 1σ range of the variation is restricted to about 2.5%–4% of the total FOV.³ Given

³ We attribute the majority of this variation to the fact that individual bright points may “blink” off for several frames before reappearing at or near their last location. The effect is unrelated to the spatial resolution in the image and is most likely an indication of the transient nature of bright points associated with magnetic elements.

that the total area coverage in the final summed map is 26%, the effect of seeing on the area coverage is therefore small.

Of special note in the final magnetic element coverage map of Figure 5*b* are the compact “voids” near the center of the FOV: regions from which MBPs are persistently excluded over the entire 70 minute time series. From examination of the *G*-band time series it is seen that the bright point pattern in these areas is constrained to large-scale rings which surround the voids. Two such rings are indicated by the circles in Figure 5. The circles are plotted at exactly the same locations in both images shown in the figure; their diameters are each 3020 km. Magnetic elements in these rings merge, fragment, and move, but stay roughly organized in the ring pattern throughout the time series. Such granular-scale rings have been seen in previous single-image *G*-band observations of active network and plage, but this is the first time series we have acquired which establishes their persistence on time scales of at least one hour.

The region defined by the final time-summed map in Figure 5*b* is fundamentally different in both flow pattern and intensity compared to the quiet Sun. Figure 7 (Plate 30) shows a single 4686 Å image from the network FOV divided into regions within and outside of the final summed bright point mask. The texture of the flow field inside the mask is highly irregular, lacking any discernible granulation. In contrast, the region outside the mask contains only normal photospheric granulation. The differences in image texture persist throughout the time series, indicating that the effect is not an artifact of the seeing. Very similar delineations in flowfield texture have been demonstrated by previous analyses in which the extent of the mask is based on mean magnetic flux measurements taken from a longitudinal magnetograms (Title et al. 1992; Topka, Tarbell, & Title 1992).

In addition to flow texture, the intensity and rms contrast of the areas within and outside the MBP time-summed mask differ markedly. Figure 8 plots the ratio of *G* band and wideband 4686 Å intensity inside the mask to the intensity outside the mask as a function of frame number (time). The wideband intensity is essentially unchanged inside and outside of the mask (mean ratio = 0.998). Conversely, the

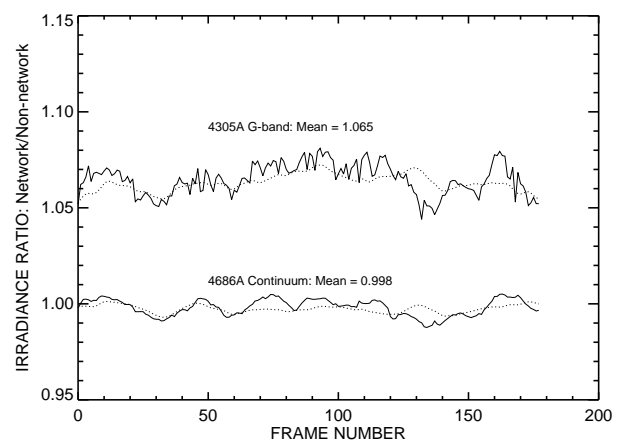


FIG. 8.—Ratio of measured intensity in the magnetic region defined by the mask in Fig. 5*b* to the intensity outside the mask as a function of frame number in the time series. Solid lines are measurements from the data prior to spacetime filtration; dotted lines show measurements after spacetime filtration.

G-band intensity is on average 6.5% higher inside the mask, principally due to the presence of the bright points. The rms contrast of the images differs as well: in the wideband images, the rms contrast inside the mask is 16% lower than outside. In the *G* band, there is an *increase* in the average rms contrast within the mask of 8%, primarily due to the existence of the MBPs. As a control, the time-summed mask was placed on an area of granulation from the quiet FOV and the intensity comparison carried out again for the *G*-band time series. The average ratio of intensity inside and outside the mask in the control case is 0.996, the mean rms contrast variation ratio is also 0.996, and there is very little temporal variation in either ratio. Table 1 summarizes the intensity and contrast comparisons.

The increase in *G*-band rms contrast within the mask agrees qualitatively with the results of Title et al. (1992) who find that in “line center” filtergrams (which exhibit bright points in association with magnetic elements) the magnetic regions exhibit a 20%–50% increase in rms contrast variation. Similarly, the wideband channel images closely resemble the continuum images of Title et al. (1992) which also exhibit a decrease in rms contrast within magnetic regions. The strong similarities in texture as well as the similarities in trends in image contrast within and outside of our mask when compared to the magnetic region mask of Title et al. (1992) lead us to conclude that the summed bright point mask of Figure 5*b* delineates the predominantly magnetic and nonmagnetic regions within the network FOV. Accordingly, we hereafter refer to the region inside the bright point mask of Figure 5*b* as the “magnetic region” of our data set.

5.2. LCT Flow Field Measurements

Prior to measuring magnetic element motions we measure flowfield properties using the well-tested method of LCT on both the *G* band and wideband datasets. The specific local correlation tracking algorithm used is as follows: rectangular image subfields or “tiles” are systematically shifted and a mean-square intensity difference metric is calculated with respect to subfields from the previous image in time. The lowest value of the difference metric (cubically interpolated to give subpixel accuracy) determines the reported displacement of the tiles. The subfields are apodized with a Gaussian window of FWHM equal to twice the width of the subfield. The initial subfield windows overlap by one-half of a tile width. The resulting LCT dataset possesses velocity measurements on a grid with spacing equal to the tile width; an LCT measurement with a FWHM of 0.8 is based on a flow grid with 0.4 resolution. All of our LCT measurements are performed on the phase-

velocity filtered dataset in accord with past applications of high-resolution LCT (Wang et al. 1995).

The LCT grid spacing and FWHM are free parameters in any LCT measurement. In our case, we fix the FWHM-to-grid ratio and vary only the grid width to achieve different measurement resolution. Measured flow speeds vary strongly as a function of the flow grid FWHM. Figure 9 plots the measured rms speed as a function of the window FWHM for the *G*-band time series, in both the network and quiet subareas. For comparison, data from the granulation time series taken with the SOUP instrument on *Spacelab 2* is shown as well (Title et al. 1989). The solid line is an empirical fit given by

$$S^{\text{rms}}(w) = S_0^{\text{rms}} \sqrt{\frac{1 + w_0^2}{1 + w^2}}, \quad (2)$$

where S^{rms} is the rms speed, w , is the FWHM of the LCT grid, and S_0 and w_0 are the reference values (chosen as the *G*-band quiet FOV values at 0.67 in the figure). The limit as w goes to zero for the fit shown is 1928 m s^{-1} .

As the FWHM of the subfield is decreased, correlation between frames becomes dominated by granular substructure which is moving significantly faster than granular or mesogranular advection speeds. Since we are interested in comparing the granular flow field on the smallest measurable scales with results of magnetic element tracking, we choose the smallest FWHM value which is not noise dominated. For both the *G*-band and wideband 4686 Å time series, this was found to be approximately 0.8 (corresponding to a flowgrid width of 0.4).

Comparison of LCT flow fields measured from the *G*-band and 4686 Å time series reveals slight, but significant, differences. Given that the images are simultaneous to less than 10 ms, and that the appearance of the granulation in the two bandpasses is qualitatively identical, the flow fields measured from the two data sets are expected to be nearly identical. However, in low-speed regions of flow speed (i.e., for speeds below about 200 m s^{-1}) the *G*-band and wideband velocity maps exhibit large differences, particularly in flow direction. We quantify the difference in the measured flow fields by calculating the correlation between velocity

TABLE 1
INTENSITY CHARACTERISTICS OF PIXELS INSIDE AND OUTSIDE OF THE MAGNETIC REGION

Region	\bar{I}_{4305}	\bar{I}_{4686}	C_{4305}	C_{4686}
Magnetic	531.52	505.00	13.70	8.73
Nonmagnetic	499.05	505.92	12.72	10.40
Ratio	1.065	0.998	1.08	0.84

NOTE.—Magnetic region is defined by the mask shown in Fig. 5*b*. \bar{I}_λ is the intensity averaged over the time series for wavelength λ (in Å) in units of DN (data numbers); C_λ is the rms contrast averaged over the time series. The ratio is the magnetic region mean value divided by the “nonmagnetic” mean value. All values are calculated from the unfiltered time series.

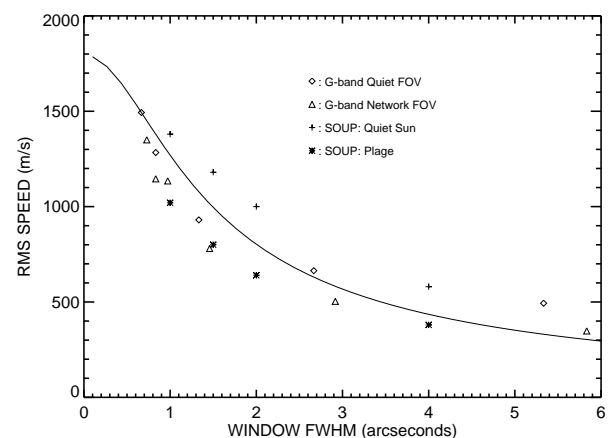


FIG. 9.—Local correlation tracking rms speed measurements as a function of the FWHM of the apodization window. Data for the SOUP instruments results are taken from Title et al. (1989). The solid line is an empirical fit constrained to the smallest FWHM value in the quiet-FOV data.

maps defined as follows:

$$R_v = \frac{\sum_i^N v_i \cdot w_i}{\sqrt{\sum_i v_i^2} \sqrt{\sum_i w_i^2}}, \quad (3)$$

where v_i and w_i are the G -band and wideband velocity vectors at flow-field gridpoint i , respectively, and N is the total number of gridpoints in a single velocity mapping. For two identical flow maps, $R_v = 1.0$. The correlation between flow fields is maximized in the quiet FOV for a FWHM of 0.8: 65% of all correlations are above 0.9; the maximum correlation is 1.0, the minimum is 0.0, and the mean value is 0.86. Decreasing the FWHM to 0.66 decreases the correlation indicating that the signal-to-noise ratio at this resolution is lower. The G -band/wideband flow-field correlation is also maximized in the network FOV for a FWHM of 0.8. As in the network FOV, decreasing the width slightly to 0.7 decreases the correlation. For both the network and the quiet subfields we choose a FWHM of 0.83 (grid spacing of 0.415) for all subsequent analyses of flow field properties.

Within the network FOV, the ensemble of all wide-band LCT speeds has modal, mean, and rms speeds of 550, 950, and 1150 m s^{-1} , respectively. In the quiet FOV the modal, mean, and rms speeds are 700, 1100, and 1300 m s^{-1} respectively. In both FOVs the speeds are well fit by Rayleigh distributions, as is expected for the magnitude of a normally distributed two-dimensional vector field. Figure 10 compares the two distributions and their respective least-square fits. While these histograms demonstrate the global character of flow-field suppression by magnetic fields in the network FOV, more specific effects can be seen by imaging the speed measurements over the fields of view.

Figure 11a (Plate 31) color codes the flow speed at every pixel in the network FOV averaged over the entire time series. The mean flow speed at a particular LCT gridpoint is calculated by averaging the displacement measurements over the full time series and dividing by the mean time between frames. Speeds at pixels not covered by an LCT gridpoint are calculated by cubic interpolation from the nearest grid points. The figure includes mean flow vectors (averaged over the entire time series) at the LCT grid points as well as contour lines which outline the magnetic region as defined Figure 5b. Clearly the highest degree of flow-field

suppression is localized to the magnetic region within the network FOV within the magnetic region, the mean flow speed is 650 m s^{-1} , while outside the region the mean flow speed is 1000 m s^{-1} .

Figure 11b (Plate 31) shows an analogous “speed image” for the quiet FOV. The LCT grid has the same FWHM as used in the network FOV and the image is scaled to the same color table. The quiet FOV has a higher range of speed values compared to the network FOV, but lacks any discernible spatial pattern. Table 2 compiles the statistics of the average flowmaps for both regions shown in Figure 11.

5.3. Magnetic Bright Point Tracking

Statistical description of magnetic element dynamics requires automated tracking of many individual objects. The object tracking method used for this study is based on measuring the centroid location of hundreds of MBPs in a time series of binary maps such as the one shown in Figures 4a and 4b. The centroid of any given MBP is measured with a precision of 0.01 pixel. Tracking of a given object is implemented by considering the time series of bright point maps as constituting a cube in spacetime: the x - and y -axes are the two-dimensional image coordinates and the z -axis represents frame index or time. In this “image cube,” objects consist of “trees” of bright point voxels growing in the time direction. Tracking a given MBP is then equivalent to segmenting its representative three-dimensional bright point tree from the image cube.

Computationally efficient segmentation of the trees is implemented using one-dimensional integer voxel addressing: for bright point voxel i located at coordinates (x_i, y_i, z_i) , the one-dimensional index is given by $\kappa_i = x_i + y_i X + z_i XY$, where X and Y are the dimensions of the cube in the x - and y -axes, respectively. For a given bright point voxel, valid neighboring voxels are sifted from a list of all known bright point voxels located only on adjacent levels. This procedure continues for all z -planes below the original plane on which an MBP is first identified until the object disappears or until the last plane in the cube is reached. Figure 12 (Plate 32) shows a single MBP that has been segmented from the image cube. Given the one-dimensional voxel addresses for an object, it is a simple matter to calculate the centroid of a two-dimensional slice on any given level. Splitting of an MBP is defined as those occurrences in which there are more centroids on level i than on level $i - 1$. Merging is detected by searching the datacube backward in time and identifying “inverse splittings.” Given a list of centroid coordinates, the displacement between frames of an MBP is calculated as the vector distance between an object’s centroid on level i and the projection onto level $i - 1$.

As mentioned in § 5.1, bright points in the maps can occasionally “blink off” and reappear in later frames.

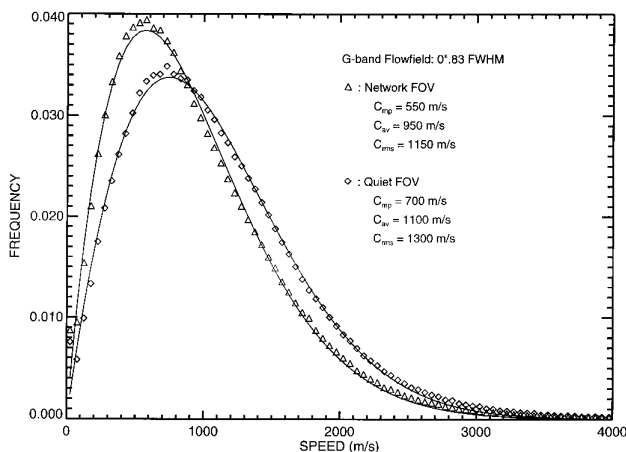


FIG. 10.—Comparison of LCT measured average speed distributions in the network and quiet subfields. The solid lines are least-square fits to Rayleigh distributions. The effect of magnetic field concentration is evidenced by the ~20 decrease in the measured speeds in the network FOV.

TABLE 2

LCT SPEED DISTRIBUTION STATISTICS FOR G -BAND TIME SERIES

FOV	Minimum	Mode	Mean	rms
Quiet	0.0	700	1100	1300
Network:				
Overall	0.0	550	950	1150
Magnetic	0.0	350	650	800
Nonmagnetic	0.0	650	1000	1200

NOTE.—FWHM = 0.8. All speeds are in units of m s^{-1} .

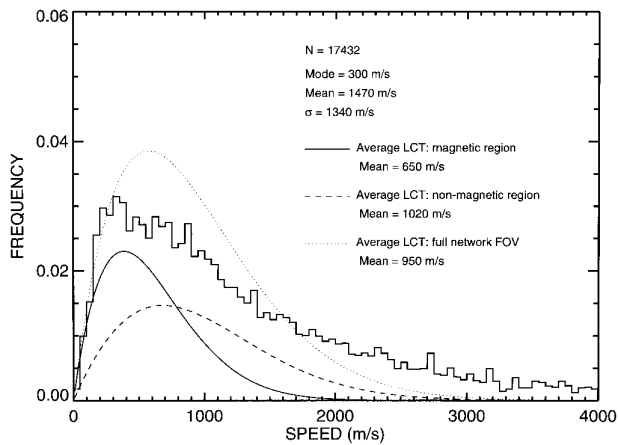


FIG. 13.—Distribution of measured magnetic element speeds (*block histogram*). Also shown are the Rayleigh distribution fits to the measured LCT speeds ($\text{FWHM} = 0.8$) segregated in three ways: the solid line indicates the LCT speed distribution derived by averaging all 178 flow fields and then masking the flow field with the “magnetic region” mask shown in Fig. 5b; the dashed line is the speed distribution of the same averaged flow field outside of the magnetic region mask; the dotted line shows the average speed distribution (derived from all 178 measured flow fields) for the entire network FOV (equivalent to the network FOV curve shown in Fig. 10).

Reappearances which occur within two frames in the time series are defined as a continuation of a given object’s track rather than the beginning of new object in the image cube. In practice, this definition is implemented by dilating the binary bright point cube with a (1, 1, 3)-voxel kernel to effectively smooth out time variability on scales less than two frames.

Automated tracking is performed on the $350 \times 350 \times 178$ element MBP binary array. Objects whose temporal extent covers less than five frames in the dataset (approximately 2 minutes) are neglected in order to reduce the chances of measuring noise structures. The temporal threshold results in 534 objects identified for measurement. The total number of displacement measurements that are greater than zero is 17432. The resulting magnetic element speed histogram is shown in Figure 13. Measured speeds above 7000 m s^{-1} (the approximate speed of sound in the photosphere) are not included in the distribution on the grounds that they are most likely due to large centroid

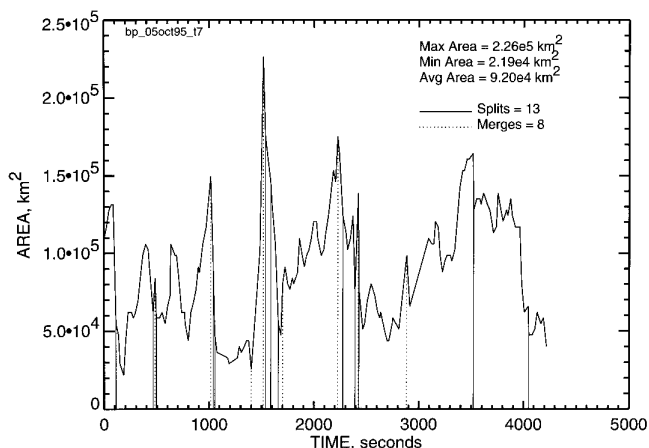


FIG. 14.—Area of a single MBP plotted as a function of time. The level of variability displayed is typical of most elements in the region. Note that not all sudden decreases or increases are correlated with observed splittings or mergers.

jumps following the merger of two magnetic elements. The measured modal and mean speeds of magnetic elements in the data set are 300 and 1470 m s^{-1} , respectively, with a standard deviation of 1340 m s^{-1} ; the median value is 1040 m s^{-1} .

Approximately 25% of the objects tracked underwent measurable splitting, meaning that the centroids of the fragments were located far enough apart to be discriminated as separate objects. The mean time between splitting is 320 s and the mean time between mergers is 404 s. The “mean interaction period,” defined as the average time between either a merging or splitting event for all elements, is therefore approximately 360 s, or 6 minutes. This is the average lifetime of granules as determined by Title et al. (1989) using autocorrelation analyses on high-resolution continuum filtergrams of quiet-Sun granulation. The power spectra of both splitting and merging times show strong peaks at 25 s (approximately the frame period of the time series), but no other significant periodicities.

Figure 14 shows a plot of measured area versus time for one of the longer-lived MBPs in the time series. Vertical lines mark the times of observed splitting or merging events for this object. This particular element underwent 13 splitting events and eight mergers over the course of the 70 minute tracking period. Note that there are several large excursions in area which are not associated with observed fragmentation or merging.

As mentioned in the introduction, we cannot accurately measure the lifetime of magnetic elements using MBPs as tracers. Nevertheless, measurements of MBP lifetimes from our data set are of interest. We define the lifetime of an MBP as the number of frames over which its corresponding three-dimensional tree can be traced through the data set. By this definition, a large bright point from which a smaller fragment diverges is considered to continue as the same object. Similarly, merging of a bright point into a preexisting tree defines the end of the bright point’s lifetime but not of the tree. For example, the lifetime of the object shown in Figure 12 is defined as 178 frames (or 70 minutes). Although it undergoes numerous split/merge interactions, some branch of the structure can be continuously followed in time throughout the dataset. By this definition of lifetime, we find that most MBPs are traceable only briefly: the modal lifetime is 2 minutes, the mean lifetime is 9.33 minutes. However, the maximum lifetime measured (for approximately 5% of all bright points tracked) is 70 minutes.

6. CONCLUSIONS

In the following, all references to the “magnetic region” refer to the area defined by the bright point travel range as shown in Figure 5b. Both the complement of this region in the network FOV and the entire quiet FOV are referred to as “nonmagnetic” regions. Although these regions are unlikely to be entirely free of magnetic flux, the term is applied for brevity.

6.1. Large-Scale Characteristics

Comparison of the G -band and 4686 \AA wideband images reveals that in addition to brightening in the cores of magnetic elements, relative G -band brightening is found in diffuse form in the magnetic region. In particular, the diffuse “emission” is strongest in regions which appear as micropores in the wide-band images. The magnetic element and

diffuse emission form a continuous distribution in contrast comparisons between *G*-band and wideband images (see Fig. 3). Micropores visible in the data set are in general smaller and have lower contrast relative to the granulation in *G*-band images when compared to the 4686 Å images. From the continuity of the contrast distribution, the spatial relationship of the diffuse emission to the magnetic element cores, and the coherent temporal evolution of the diffuse areas we conclude that the diffuse component is a magnetic field effect on *G*-band radiation transfer in the photosphere and not a instrumental or atmospheric artifact.

The 4686 Å wideband intensity is unchanged between the magnetic and nonmagnetic regions. For comparison, Title et al. (1992) find that in clean continuum at 6303.2 Å, magnetic regions are on average 1.5% darker than nonmagnetic regions, primarily due to the presence of micropores. The discrepancy is most likely due to the large number of lines in our relatively wide bandpass (54 Å vs. 0.070 Å) resulting in line-center brightening in magnetic elements. Similarly, the 6.5% average increase in *G*-band intensity in the magnetic region is due to the strong brightening of magnetic elements in this bandpass. This is to be compared with the ~5% increase in plage intensity measured in Ni I 6768 Å line center images by Title et al. (1992).

6.2. Flow Field Measurements

LCT results are highly dependent on the spatial and temporal resolution of the underlying measurement grid. Figure 9 shows this effect well and in addition confirms the LCT results of Title et al. (1989). The implications are that LCT is capable of measuring a wide range of flow speeds, from relatively fast “granular fragments” to the slower “advection” speeds of 300 m s⁻¹ or less; the term “characteristic speed” must be used only in relation to a given spatiotemporal resolution. As a caveat, it is important to mention that LCT measurements strictly apply only to the *brightness* patterns in the time series and not necessarily to mass flows. It is conceivable, though not highly probable, that mass flow vectors on scales of several hundred km in the photosphere may differ from the flow vectors derived from LCT brightness measurements.

In verification of our LCT measurements, we find good agreement of the absolute magnitudes with values measured on comparable high-spatial resolution granulation time series. In particular, Wang et al. (1995) find a modal speed about 650 m s⁻¹ in a quiet granulation region using an apodization window of 1" FWHM. Given the similarity in grid resolution, this agrees well with the modal value of 700 m s⁻¹ we find in our quiet FOV.

Suppression of flow speeds by magnetic fields are found to be highly localized within the network FOV. Title et al. (1992), comparing the difference between plage magnetic field regions and quiet Sun, find a similarly sharp delineation between “magnetically suppressed” flow and normal flow in LCT measurements. They measure a speed suppression of about a factor of 2 in the plage using an LCT FWHM of 2", somewhat higher than the factor of 1.6 (650 magnetic vs. 1000 nonmagnetic) that we measure here. The discrepancy may be due to the higher magnetic element density within plage regions compared to the active network region studied here.

We summarize the flow speed suppression due to magnetic fields as follows: define \bar{C}_q as the mean measured speed in the quiet FOV, \bar{C}_n as the mean speed in the

network FOV, $\bar{C}_{n,\text{nonmag}}$ as the mean speed in the network FOV *outside* of the magnetic region, and $\bar{C}_{n,\text{mag}}$ as the mean speed in the network FOV *inside* the magnetic region. Then the analyses § 5.2 show that in general

$$\bar{C}_q \approx \bar{C}_{n,\text{nonmag}} > \bar{C}_n \gg \bar{C}_{n,\text{mag}} . \quad (4)$$

Specifically,

$$\bar{C}_q \approx 1.09 \bar{C}_{n,\text{nonmag}} , \quad (5)$$

$$\bar{C}_q \approx 1.6 \bar{C}_{n,\text{mag}} , \quad (6)$$

The fact that we find a 9% flow speed suppression relative to the quiet FOV even outside of the magnetic region may indicate that there is a significant amount of magnetic flux outside of our defined region. Conversely, there may be little magnetic flux outside of the region but the effect of the magnetic field may extend into the nonmagnetic flowfield by some distance. The latter hypothesis is consistent with Title et al. (1992) who find that the effects of plage magnetic fields on the flow character extend somewhat beyond the relatively sharp magnetic field boundary defined by their magnetogram threshold.

Another clear delineation between flow fields within and outside magnetic regions is found by simulating the motion of particles displaced by the measured LCT flows. Figure 15 (Plate 33) shows such a simulation based on the 0".8 FWHM LCT flow field in the network FOV. The particles, or “corks” (so called because they are imagined to “float” on the surface flowfield), are shown as white crosses on a gray-scale *G*-band image. The initial frame is solid white because we trace 122,500 corks located at every pixel of the first image in the time series. The figure shows only 12 frames from the full 178 frame simulation. The position of the corks at time $t_i = t_{i-1} + \Delta t$ is determined by adding to their location at time t_{i-1} the LCT flow vector measured between times t_{i-1} and t_i . Corks are allowed to overlap in this simulation so that we track all 122,500 corks at all times except in the case where a particle is displaced outside of the FOV; in that case, the particle is lost to the simulation. The value of Δt in the space-time filtered LCT data set used for the simulation is 23.5 s.

The resulting sequence of images clearly shows that outside of the magnetic region, the flow field transports corks to the boundaries of cells on the order of 5"–10" in diameter. These cells are nearly fully delineated after about 30 minutes of simulated flow, but the cells continue to evolve via merging or collapse of neighboring cells throughout the time series. Compared to the chaotic flow on granular scales these “mesogranular” scale cells are fairly stable over times on the order of 10 min. In contrast, Figure 15 shows that within the magnetic region there is very little cork motion over the entire 70 minutes of the series. Not surprisingly, there are no mesogranular-scale cells within the magnetic region. This again emphasizes that while the magnetic elements identified by *G*-band bright points in any one of our images occupy only 3%–4% of the area, the flow field is effected over (at least) the much larger “magnetic region” defined in Figure 5b.

For comparison to Figure 15, Figure 16 (Plate 34) shows the equivalent time series of cork flow images for the quiet FOV. In the (apparent) absence of concentrated magnetic flux, the entire FOV is covered by mesogranular cells which are well delineated and relatively stable after approximately 30 minutes of simulated cork flow. There is some indication

that the mesogranules in the quiet FOV are somewhat larger than those in the nonmagnetic region of the network FOV. However, the limited length of our time series prevents any definite conclusions based on these cork-flow simulations.

In an attempt to further quantify the mesogranular cell structure of the cork simulations we calculate flow-field divergence and curl from the LCT velocity measurements. Divergence (or convergence) of the mean flow field is calculated as the directional gradient of the mean LCT vectors and is illustrated in Figure 17 (Plate 35). As in Figure 11, we calculate the divergence values at the discrete LCT grid points and then cubically interpolate the values to cover the entire FOV. The maps are shown overlaid by the mean flow-field vectors measured at the grid points; both figures are displayed to the same color scale. Regions of positive divergence (relative outflow) are white and regions of negative divergence (relative inflow) are shown red to black. The mean divergence in both fields of view is effectively zero (below 10^{-5} s^{-1} in both cases). Both fields have maximum divergence values of 0.32 s^{-1} located at the center of mesogranular cells. The network FOV has a minimum of -0.25 s^{-1} , while the quiet FOV minimum is -0.32 s^{-1} .

6.3. Magnetic Element Motion⁴

The majority of MBP speeds measured are consistent with the suppressed horizontal velocities measured using LCT. In particular, most of the measured magnetic element speeds are a factor of 2 lower than the mean LCT speeds in the magnetic region. However, comparing the peaks of the histograms in Figure 13 it is evident that the modal LCT speed and the modal MBP speeds are nearly equivalent. Conversely, the MBP speed histogram has a large high-speed tail which is lacking from the magnetic region LCT data. The high-speed tail of the MBP distribution exceeds that of even the nonmagnetic LCT distribution. We conclude that most of the time MBP motions are commensurate with the suppressed granular flows in the magnetic region but are occasionally driven to speeds on the order of $1\text{--}2 \text{ km s}^{-1}$ under the influence of more active flows.

The mean MBP speed of 1470 m s^{-1} compares well with measurements from past studies of magnetic element dynamics. For instance, manual tracking of MBPs in a moat region outside a sunspot penumbra resulted in mean speeds of $1\text{--}2 \text{ km s}^{-1}$ (Berger & Title 1996). Similarly, Muller et al. (1994) report mean and modal speeds of 1.33 and 1.0 km s^{-1} , respectively, for isolated magnetic elements in quiet Sun. The modal speed measured in this study is approximately 3 times larger than the 300 m s^{-1} we measure in the current study. This supports the hypothesis that MBPs in quiet Sun areas or on the boundaries of magnetic regions are subject to higher velocity flow fields compared to MBPs within magnetic regions.

The fact that the mean interaction time of 360 s is equal to the average lifetime of granulation further supports the hypothesis that local granular motions drive the most energetic magnetic element motions. The lack of periodicity in the splitting data argues against any periodic forcing

mechanisms that might be proposed for magnetic element evolution, such as *p*-mode acoustic forcing. However, it does not rule out random acoustic forcing as a mechanism. Using the mean speed measurement, the interaction time can be used to calculate a “mean free path” of magnetic elements in an enhanced network of about 530 km; about twice the typical MBP diameter.

The 9.3 minute average lifetime of MBPs that we measure here is consistent with measurements of network bright point (NBP) average lifetimes (Muller 1994). However, we find some bright points persisting for up to 70 minutes, far greater than the maximum 20 minutes reported by Muller (1994). Also, the percentage of magnetic elements that measurably split (25%) is much higher than found by Muller et al. (1994) who state that NBPs undergo splitting only rarely. In addition, the ring structures in Figure 5 demonstrate that not only individual bright points but *patterns* of flux organization can have lifetimes significantly longer than those measured for quiet-Sun magnetic elements. These discrepancies are likely due to the greater density of magnetic elements in our enhanced network region relative to the quiet-Sun regions used to study NBPs.

Further investigation is required in order to discern the long timescale evolution of network flux in the photosphere as well as the relation of surface flux elements to (presumably) larger magnetic structures below the surface. These investigations require at least two additional data sets. First, a phase-diversity corrected *G*-band time series (ideally of several hours in length) with simultaneous 4686 Å and magnetogram images. Such a data set will allow much more quantitative analysis of the underlying magnetic flux in relation to the fraction of magnetic elements which appear as *G*-band bright points. The SVST is equipped for such observations and we obtained a suitable data set in the summer of 1997. Second, measurements of sub-surface magnetic structure and dynamics with simultaneous observations of surface dynamics. Analyses of subsurface flow-field structures based on helioseismic techniques (Duvall et al. 1997) are currently under development. We plan to undertake simultaneous observations using the SoHO/MDI instrument and the SVST in order to begin to develop the analysis tools for relating surface LCT measurements to subsurface flow fields. However, investigation of small-scale magnetic field dynamics below the surface will require a significant increase in the spatial resolution of helioseismology measurements.

This work was supported by NASA contracts NAS5-30386 at Stanford and NAS8-39747 and Independent Research Funds at Lockheed-Martin. M. G. L. was supported by the Swedish Science Research Council. Göran Scharmer, Karel Schrijver, Ted Tarbell, Mandy Hagenaar, and Kees Zwaan provided helpful comments and suggestions. Darrel Torgerson designed the optical layout of our instrumentation at the SVST. The SVST is operated by the Swedish Royal Academy of Sciences at the Spanish Observatorio del Roque de los Muchachos of the Instituto de Astrofísica de Canarias (IAC). Paco Armas, Göran Hosinsky, Rolf Keiser, and Wang Wei of the Swedish Solar Observatory maintain the SVST in its status as one of the premiere solar telescopes in the world. The staff of the IAC are thanked for providing excellent accommodations and assistance during observations on La Palma.

⁴ We remind the reader that our analyses rely entirely on measurements from *G*-band bright points. As discussed in the § 2, this results in inherent biases in the analyses and requires caution when formulating conclusions applicable to the magnetic field.

REFERENCES

- Auffret, H., & Muller, R. 1991, *A&A*, 246, 264
 Beckers, J. M., & Schröter, E. H. 1968, *Sol. Phys.*, 4, 142
 Berger, T. E. 1996, Ph.D. thesis, Stanford Univ.
 Berger, T. E., Schrijver, C. J., Shine, R. S., Tarbell, T. D., Title, A. M., & Scharmer, G. 1995a, *AJ*, 454, 531
 Berger, T. E., Shine, R. S., Title, A., Tarbell, T. D., & Scharmer, G. 1995b, *BAAS*, 27, 1426
 Berger, T. E., & Title, A. M. 1996, *ApJ*, 463, 365
 Bogart, R. S., Ferguson, S. H., Scherrer, P. H., Tarbell, T. D., & Title, A. M. 1988, *Sol. Phys.*, 116, 205
 Dunn, R. B., & Zirker, J. B. 1973, *Sol. Phys.*, 33, 281
 Duvall, T. L., Jr., et al. 1997, *Sol. Phys.*, 170, 63
 Keller, C. U. 1992, *Nature*, 359, 307
 ———. 1993, in *ASP Conf. Ser. 46, The Magnetic and Velocity Fields of Solar Active Regions*, ed. H. Zirin, G. Ai, & H. Wang (San Francisco: ASP), 3
 Keller, C. U., Solanki, S. K., Tarbell, T. D., Title, A. M., & Stenflo, J. O. 1990, *A&A*, 236, 250
 Löfdahl, M. G. 1996, Ph.D. thesis, Stockholm Univ.
 Löfdahl, M. G., Berger, T. E., Shine, R. A., & Title, A. M. 1998, *ApJ*, 495, 965 (Paper I)
 Löfdahl, M. G., & Scharmer, G. B. 1994, *A&AS*, 107, 243
 Mehlretter, J. P. 1974, *Sol. Phys.*, 38, 43
 Muller, R. 1985, *Sol. Phys.*, 100, 237
 ———. 1994, *Solar Surface Magnetism*, ed. R. J. Rutten & C. J. Schrijver, NATO ASI Series C, vol. 433 (Dordrecht: Kluwer), 73
 Muller, R., & Keil, S. L. 1983, *Sol. Phys.*, 87, 243
 Muller, R., & Mena, B. 1987, *Sol. Phys.*, 112, 295
 Muller, R., & Roudier, T. 1992, *Sol. Phys.*, 141, 27
 Muller, R., et al. 1994, *A&A*, 283, 232
 November, L. J. 1986, *Appl. Opt.*, 25, 392
 November, L. J., & Simon, G. W. 1988, *ApJ*, 333, 427
 Parker, E. N. 1990, in *Mechanisms of Chromospheric and Coronal Heating*, ed. P. Ulmschneider & E. R. Priest (Berlin: Springer), 615
 Rabin, D. 1992, *ApJ*, 390, L103
 Roudier, T., Espagnet, O., Muller, R., & Vigneau, J. 1994, *A&A*, 287, 982
 Solanki, S. K. 1993, *Space Sci. Rev.*, 63, 1
 Spruit, H. C., & Zwaan, C. 1981, *Sol. Phys.*, 70, 207
 Stenflo, J. O. 1973, *Sol. Phys.*, 32, 41
 Tarbell, T. D., Title, A. M., & Schoolman, S. A. 1979, *ApJ*, 229, 387
 Title, A. M., & Berger, T. E. 1996, *ApJ*, 463, 797
 Title, A. M., et al. 1989, *ApJ*, 336, 475
 ———. et al. 1990, in *Physics of Magnetic Flux Ropes*, ed. C. T. Russell, E. R. Priest, & L. C. Lee, *Geophys. Monogr.* 58 (Washington, DC: AGU), 171
 Title, A. M., Topka, K. P., Tarbell, T. D., Schmidt, W., Balke, C., & Scharmer, G. 1992
 Topka, K. P., Tarbell, T. D., & Title, A. M. 1992, *ApJ*, 396, 351
 Wang, Y., Noyes, R. W., Tarbell, T. D., & Title, A. M. 1995, *ApJ*, 447, 419
 Yi, Z., & Engvold, O. 1993, *Sol. Phys.*, 144, 1
 Zayer, I., Solanki, S. K., & Stenflo, J. O. 1989, *A&A*, 211, 463